Atomistic Modeling of Short Pulse Laser Ablation of Metals: Connections between Melting, Spallation, and Phase Explosion†

Leonid V. Zhigilei,* Zhibin Lin,‡ and Dmitriy S. Ivanov§

Department of Materials Science and Engineering, University of Virginia, 395 McCormick Road, Charlottesville, Virginia 22904-4745

Received: March 14, 2009; Revised Manuscript Received: May 4, 2009

The mechanisms of short pulse laser interactions with a metal target are investigated in simulations performed with a model combining the molecular dynamics method with a continuum description of laser excitation, electron−phonon equilibration, and electron heat conduction. Three regimes of material response to laser irradiation are identified in simulations performed with a 1 ps laser pulse, which corresponds to the condition of stress confinement: melting and resolidification of a surface region of the target, photomechanical spallation of a single or multiple layers or droplets, and an explosive disintegration of an overheated surface layer (phase explosion). The processes of laser melting, spallation, and phase explosion are taking place on the same time scale and are closely intertwined with each other. The transition to the spallation regime results in a reduction of the melting zone and a sharp drop in the duration of the melting and resolidification cycle. The transition from spallation to phase explosion is signified by an abrupt change in the composition of the ejected plume (from liquid layers and/or large droplets to a mixture of vapor-phase atoms, small clusters and droplets), and results in a substantial increase in the duration of the melting process. In simulations performed with longer, 50 ps, laser pulses, when the condition for stress confinement is not satisfied, the spallation regime is absent and phase explosion results in smaller values of the ablation yield and larger fractions of the vapor phase in the ejected plume as compared to the results obtained with a 1 ps pulse. The more vigorous material ejection and higher ablation yields, observed in the simulations performed with the shorter laser pulse, are explained by the synergistic contribution of the laser-induced stresses and the explosive release of vapor in phase explosion occurring under the condition of stress confinement.

1. Introduction

Short pulse laser ablation is the phenomenon that is actively used in a broad range of applications, from surface micromachining[1,2] and pulsed laser deposition of thin films and coatings[3] to the design of laser plasma thrusters for small satellites.[4] The mechanisms responsible for the material removal in laser ablation include an intensive evaporation from the irradiated surface at low laser fluences and/or long pulse durations,[5] an explosive decomposition of a surface region of the target into individual atoms or molecules and liquid droplets at higher fluences,[6−9] hydrodynamic sputtering[10,11] or expulsion of molten material due to the action of the evaporation or ablation recoil pressure,[12−14] an ejection of large droplets or fractured solid fragments caused by photomechanical effects,[15−18] as well as nonthermal processes related to photochemical reactions[19,20] or laser-induced charging and Coulomb explosion of a surface layer of the target.[21]

The explosive boiling or "phase explosion", in particular, is commonly discussed as a primary mechanism of short pulse laser ablation of metal targets,[6−9,22−24] where the surface charging and Coulomb explosion are inhibited by the high mobility of the conduction band electrons.[21] This mechanism of material ejection involves an explosive decomposition of a surface region of the target superheated beyond the limit of thermodynamic stability of the target material (~90% of the critical temperature) into a two-phase mixture of liquid and vapor. Experimental observations of the onset of the ejection of liquid droplets as well as a steep increase in the ablation rate are often interpreted as evidence of the transition from normal vaporization to phase explosion.[9,22,24,25] The results of hydrodynamic modeling[26,27] and molecular dynamic (MD) simulations[17,23,28−31] of short pulse laser ablation confirm phase explosion as the dominant mechanism responsible for the material ejection at laser fluences below the values leading to substantial ionization and plasma formation. The results of MD simulations, in particular, provide detailed information on the dynamics of the explosive decomposition of the overheated surface region and characteristics of the ablation plume.

The fast rate of energy deposition in short pulse laser irradiation not only leads to a sharp temperature rise in the absorbing region of the target but may also result in the generation of compressive stresses.[15] The interaction of the laser-induced compressive stresses with free surfaces of the irradiated targets can transform them into tensile stresses of sufficient strength to cause mechanical fracture of a solid material or disruption and sputtering of a melted layer. The ejection of large liquid droplets or solid particulates caused by the relaxation of the laser-induced stresses is often called photomechanical ablation or spallation.[15−17,32,33] The maximum values of the laser-induced stresses and contribution of photomechanical effects to the material ejection or damage are defined by the relationship

* Author to whom correspondence should be addressed. E-mail: lz2n@virginia.edu.

† Part of the "Hiroshi Masuhara Festschrift".

‡ Present address: Department of Physics, Texas A&M University, College Station, Texas 77843.

§ Present address: Department of Physics and the Optimas Research Centre, Technical University of Kaiserslautern, 67653 Kaiserslautern, Germany.

10.1021/jp902294m CCC: $40.75
Published on Web 06/08/2009

between the characteristic time of the laser heating and the time required for the mechanical relaxation (expansion) of the heated volume, τ_s. When the time of the laser heating is shorter than τ_s, the heating and melting take place under a nearly constant volume condition, causing a build up of compressive stresses. In short pulse laser interactions with metals, the time of the laser heating is defined by the laser pulse duration, τ_p, or the characteristic time of the energy transfer from the excited electrons to the lattice, $\tau_{e\text{-}ph}$, whichever is longer. The condition for the generation of compressive stresses, usually referred to as the condition of stress confinement,[15−17,32] can in this case be formulated as[16]

$$\max\{\tau_p,\tau_{e\text{-}ph}\} \leq \tau_s \approx L_c/C_s \quad (1)$$

where max{...} denotes the selection of the largest value of the two time constants, L_c is the diffusive/ballistic penetration depth of the excited electrons during the time of the electron−phonon equilibration, and C_s is the speed of sound in the target material.

Typically, photomechanical effects and spallation are discussed in connection with the observation of laser-induced damage and material removal at energy densities significantly below the ones needed for the explosive boiling of the irradiated material.[15,18,32,33] The results of MD simulations of laser ablation of molecular targets performed in the regime of stress confinement,[17,29,30] however, suggest that the contribution of thermoelastic stresses can also significantly affect the ablation yield and parameters of the ejected plume at laser fluences above the threshold for the onset of explosive boiling. More numerous clusters with higher ejection velocities are produced by phase explosion in the regime of stress confinement as compared to simulations performed at the same laser fluences but with longer pulses, away from the stress confinement conditions. In this case, the release of the vapor phase and relaxation of the laser-induced thermoelastic stresses are two processes acting in concert to cause the material ejection.

Transient melting and resolidification of a surface layer are processes that may also strongly affect the ablation efficiency and quality of surface structures generated by laser micromachining. It is well-established that the expulsion of the molten material under the action of the ablation recoil pressure[1,2,12,13] is playing an important, if not dominant, role in material removal with nanosecond and longer pulses of sufficiently high intensity. While ensuring high energy efficiency of the material removal, the recoil-induced expulsion of the melt also results in poor quality and low precision in laser drilling or micromachining applications. In the case of shorter (picosecond and femtosecond) pulses, surface morphology related to the melting and redistribution and/or sputtering of the melted material can be significantly reduced[34−37] to the extent that the subpicosecond laser ablation is sometimes described as "melting-free."[38] A close examination of surface morphologies in targets irradiated with picosecond and femtosecond pulses, however, suggests that melting, redistribution of the melted material to the edges of the laser spot, and possibly expulsion of the melt are taking place even in femtosecond laser ablation. In particular, the observations of crown-like rims of solidified material around the laser spots in single pulse experiments[35,39,40] or holes drilled by multipulse laser irradiation[14,18,37] as well as the complex frozen structures created by femtosecond laser irradiation of metal thin films[41−43] below the ablation threshold are clear manifestations of the active flow of the melted material before the resolidification. Recent observation of a pronounced plasma emission enhancement in dual pulse femtosecond laser ablation of Cu and Si has been attributed to melting of a surface region of the target by the first pulse, resulting in greater localization of the energy deposited by the second pulse in the melted layer.[44]

The rates of cooling and resolidification are also playing an important role in defining the morphology of the resolidified surface and contribution of the melt expulsion to the total amount of the ablated material. Geometrical limitations imposed on the heat transfer, such as two-dimensional lateral heat transfer in thin metal films,[41−43,45,46] or relatively low thermal conductivity of nonmetallic targets[37,40] are the factors that can prolong the time to complete resolidification and facilitate the effects associated with the melt redistribution and expulsion.

The processes of short pulse laser melting and material removal due to the photomechanical spallation or explosive boiling are taking place in the same time domain and are closely intertwined with each other. The partitioning of the deposited laser energy between the energy spent on the material ejection and residual thermal energy transferred to the target,[47,48] in particular, is the key factor defining the maximum depth of melting and kinetics of the resolidification process. The flow of the melted material can, in turn, lead to additional material ejection through the melt expulsion under the action of the ablation recoil pressure, thus making a major contribution to the ablation yield. A clear understanding of the interrelation among the processes of melting, resolidification, photomechanical spallation, and phase explosion is, therefore, required for a reliable theoretical description of the short pulse laser ablation phenomenon and interpretation of experimental observations. In this paper, we use the results of MD simulations of short pulse laser interactions with a bulk Ni target to perform a systematic analysis of the connections between the various processes responsible for laser ablation and target modification in laser processing. The range of laser fluences and values of pulse duration used in the simulations are chosen to cover different regimes of material response to laser heating, from melting and resolidification, to photomechanical spallation, and to explosive boiling of the overheated material. The conditions leading to the transitions between the different regimes are established, and the fluence dependence of the melting depth, time to resolidification, ablation yield, and ablation plume composition are analyzed. A brief description of the computational model used in the simulations is given in Section 2. The results of the simulations are presented and discussed in Section 3 and are summarized in Section 4.

2. Computational Model

A relatively small depth of the region where the processes of melting, photomechanical damage, and ablation are taking place in short pulse laser interaction with metals, combined with fast growth of the available computing resources, makes this phenomenon amendable to large-scale MD simulations. In order to take advantage of the predictive capabilities of MD simulations for investigation of laser interactions with metals, however, the MD technique has to be modified to incorporate a realistic description of the laser energy absorption by the conduction band electrons, relaxation and thermalization of the absorbed laser energy, and fast electron heat conduction to the bulk of the irradiated target.

To enable atomic-level simulations of processes involving electronic excitation of metal targets by short pulse laser irradiation, a hybrid atomistic−continuum model, combining the classical MD method with a continuum description of the laser excitation and subsequent relaxation of the conduction band electrons, based on the so-called two-temperature model[49]

(TTM) has been developed.[16,50] In the original TTM, the time evolution of the lattice and electron temperatures, T_l and T_e, is described by two coupled nonlinear differential equations. In the combined TTM-MD method, MD substitutes the TTM equation for the lattice temperature in the surface region of the target, where active processes of laser melting, resolidification, and/or ablation take place. The diffusion equation for the electron temperature is solved by a finite difference method simultaneously with MD integration of the equations of motion of atoms, so that the combined method can be described by the following equations.

Electrons:

$$\text{[TTM]} \quad C_e(T_e)\frac{\partial T_e}{\partial t} = \frac{\partial}{\partial z}\left(K_e(T_e)\frac{\partial}{\partial z}T_e\right) - G(T_e - T_l) + S(z,t) \quad (2)$$

Lattice:[51]

$$\text{[MD]} \quad m_i\frac{d^2\vec{r}_i}{dt^2} = \vec{F}_i + \xi m_i\vec{v}_i^T,$$

$$T_l^{\text{cell}} = \sum_{i=1}^{N^{\text{cell}}} m_i(\vec{v}_i^T)^2/(3k_B N^{\text{cell}}) \quad \text{for } z > z_{MD} \quad (3)$$

$$\text{[TTM]} \quad C_l(T_l)\frac{\partial T_l}{\partial t} = G(T_e - T_l) \quad \text{for } z < z_{MD} \quad (4)$$

where C_e is the electron heat capacity, K_e is the electron thermal conductivity, G is the electron−phonon coupling factor, C_l is the lattice heat capacity, and $S(z,t)$ is the source term used to describe the local laser energy deposition per unit area and unit time during the laser pulse. Because the laser spot size is typically much larger than the depth affected by the laser heating, a one-dimensional version of the TTM equations, eqs 2 and 4, is used in this work, with z axes directed normal to the surface of the irradiated target. The coupled TTM-MD calculations are performed for the top part of the target, up to the depth of z_{MD}, whereas in the deeper part of the computational system, the electronic heat conduction and energy exchange between electrons and lattice are described by conventional TTM.

In the MD part of the model, m_i and $\vec{r}_i$ are mass and position of atom i, $\vec{F}_i$ is the force acting on atom i due to the interatomic interactions. The cells in the finite difference discretization are related to the corresponding volumes of the MD system, and local lattice temperature, T_l^{cell}, is calculated for each cell from the average kinetic energy of the thermal motion of atoms that belong to this cell. Thermal velocity of an atom is defined as $\vec{v}_i^T = \vec{v}_i - \vec{v}^c$, where $\vec{v}_i$ is the actual velocity of an atom i, and $\vec{v}^c$ is the velocity of the center of mass of a cell to which atom i belongs. An additional term, $\xi m_i\vec{v}_i^T$, is added to the ordinary MD equations of motion to account for the energy exchange between the electrons and lattice due to the electron−phonon coupling. The coefficient ξ is calculated for each cell and at each time step of the integration of the MD equations of motion based on the values of local electron and lattice temperatures. A derivation of an expression defining coefficient ξ is given in ref 50. The expansion, density variation, and at higher fluences, disintegration of the irradiated target predicted in the MD part of the model are accounted for in the continuum part of the model, through the corresponding changes of the parameters in eq 2.[50]

In this work, the TTM-MD model is used for simulation of laser melting and ablation of a bulk Ni target. The MD part of the TTM-MD model represents the top 100 nm surface region of the target at low laser fluences, when the laser-induced processes are limited to melting and resolidification, and a 200 nm region at higher fluences, in the ablation regime. The lateral dimensions of the MD computational system are 3.53 nm × 3.53 nm, with 113600 and 227200 atoms in the 100 and 200 nm systems, respectively. Periodic boundary conditions are applied in the lateral directions, parallel to the (100) free surface of the initial fcc crystals. Before applying laser irradiation, the initial systems are equilibrated at 300 K.

As briefly discussed in the introduction, short pulse laser irradiation can induce strong pressure gradients in the surface region of the target, leading to the generation of a pressure wave propagating from the surface to the bulk of the target. In order to avoid reflection of the pressure wave from the bottom of the MD region, a dynamic pressure-transmitting boundary condition[52,53] is applied at $z = z_{MD}$. The position of the boundary layer, z_{MD}, is not fixed during the simulations but undergoes small displacements associated with the propagation of the laser-induced pressure wave through the boundary layer. The boundary condition simulates nonreflecting propagation of the laser-induced pressure wave from the surface region of the target represented by the MD method to the bulk of the target. The energy carried away by the pressure wave is monitored, allowing for control over the total energy conservation in the combined model. In the continuum part of the model, beyond the MD region, the electronic heat conduction and energy exchange between electrons and lattice are described by the conventional TTM, eqs 2 and 4. The size of the continuum region is chosen to be 1 μm, which ensures that no significant changes in the electron and lattice temperatures are observed at the bottom of the continuum region during the time of the simulations.

The thermal and elastic properties of the lattice, such as the lattice heat capacity, elastic moduli, coefficient of thermal expansion, melting temperature, entropy of melting and vaporization, etc., are all defined by the interatomic interaction potential, described in this work by the embedded atom method (EAM) in the form suggested in ref 54. Some of the parameters of the model EAM Ni material are reported in ref 50. The temperature dependence of the lattice heat capacity, $C_l(T_l)$, obtained for the model EAM Ni material, is approximated by a polynomial function and is used in the TTM equation for the lattice temperature. The increase in the value of the heat capacity at zero pressure, predicted with the EAM potential, is from 26 J K^{-1} mol^{-1} at 300 K to 36 J K^{-1} mol^{-1} at the melting temperature of the EAM Ni (~1439 K),[50] which is in a good agreement with the experimental variation of the heat capacity from 26 J K^{-1} mol^{-1} at 300 K to 36 J K^{-1} mol^{-1} at 1500 K (13% below the experimental melting temperature of 1726).[55]

The parameters used in the TTM equation for the electron temperature are listed below.[50] The electron heat capacity is $C_e = \gamma T_e$ with $\gamma = 1065$ Jm^{-3} K^{-2}, the thermal conductivity is $K_e = K_0 T_e/T_l$ with $K_0 = 91$ Wm^{-1} K^{-1}, the electron−phonon coupling factor is $G = 3.6 \times 10^{17}$ Wm^{-3} K^{-1}, and the optical absorption depth is $L_p = 13.5$ nm. Recent theoretical analysis of the electron temperature dependence of the thermophysical properties of metals under conditions of short pulse laser irradiation predicts significant deviations from the commonly used approximations of a constant electron−phonon coupling and linear electron temperature dependences of the electron heat capacity and thermal conductivity.[56] For Ni, in particular, thermal excitation of electrons from the high density of states

d band to the much lower density of states s band are found to result in a significant decrease in the strength of the electron−phonon coupling as well as in negative deviations of the electron heat capacity and electron thermal conductivity from the linear temperature dependences.[56,57] Because most of the results reported in this paper had been obtained before the data on the modified electron temperature dependences became available, the conventional assumptions of the constant electron−phonon coupling and linear temperature dependences of the electron heat capacity and thermal conductivity were used in this work. The modifications of the thermophysical properties, suggested in refs 56, 57, would affect some of the quantitative predictions of the simulations (such as the values of the threshold fluences for melting, spallation, and ablation) but would not change the qualitative physical picture of the laser-induced processes revealed in the simulations.

Irradiation by 1 and 50 ps laser pulses is represented through the source term $S(z,t)$ in eq 2, which has a Gaussian temporal profile and an exponential attenuation of laser intensity with depth under the surface (Beer−Lambert law). To ensure complete deposition of the energy of the laser pulses in the simulations, we shifted the peak intensities of the Gaussian laser pulses to 2.5 and 125 ps from the beginning of the simulations performed with 1 and 50 ps pulses, respectively. The two values of the laser pulse width are chosen to investigate the effect of stress confinement on the laser-induced structural and phase transformations. Indeed, for Ni, the values of the characteristic time of the electron−phonon equilibration, penetration depth of the excited electrons before the electron−phonon equilibration, and speed of sound predicted with the EAM potential are $\tau_{e\text{-}ph} \approx 5$ ps (ref 50), $L_c \approx 50$ nm (ref 58), and $C_s \approx 5080$ m/s (ref 59). Using these values in eq 1, one can conclude that the condition for stress confinement is satisfied for $\tau_p = 1$ ps but not for $\tau_p = 50$ ps.

The absorbed laser fluence rather than the incident fluence is used in the discussion of the simulation results. The range of absorbed laser fluences used in the simulations, from 21.5 mJ/cm^2 to 408.5 mJ/cm^2, is chosen to cover different regimes of material response to laser energy deposition, from the thermoelastic expansion and cooling of the crystalline target to the explosive boiling of the overheated surface region. At the highest fluence used in the simulations, 408.5 mJ/cm^2, the maximum temperature in the irradiated target exceeds the estimated critical temperature of the material by ∼20%. The equilibrium degree of ionization, estimated using the Saha equation for this maximum temperature and the corresponding density observed in the simulation, is less than 1%, making the effect of the ionization on the material ejection negligible. The level of ionization, however, quickly rises as the temperature increases above the critical temperature. Therefore, further extension of the simulations to higher fluences would make it necessary to include a description of the ionization into the model.

3. Results and Discussion

In this section, the results of the simulations of laser interaction with a bulk Ni target are presented first for a laser pulse width of 1 ps and a broad range of laser fluences, covering the regimes of laser melting, photomechanical spallation, and phase explosion of an overheated surface region of the target. The physical conditions leading to the transition from the photomechanical spallation to phase explosion are investigated and the connections between the maximum melting depth and processes responsible for the material removal (ablation) are discussed. The results from a series of simulations performed with longer, 50 ps, laser pulses are also presented, addressing the characteristics of the laser melting and ablation processes in the absence of stress confinement.

3.1. From Melting to Spallation and Phase Explosion. The results of four representative simulations performed for a Ni target irradiated by 1 ps laser pulses of different intensities are illustrated in Figure 1 by contour plots showing the temporal and spatial evolution of the lattice temperature and pressure. These simulations represent different types of material response to the short pulse laser irradiation, from the fast laser melting and resolidification (Figure 1a), to photomechanical separation (spallation) of a single layer of liquid material (Figure 1b), to the spallation of multiple layers or droplets (Figure 1c), and to the phase explosion of an overheated surface region (Figure 1d). Below, we provide a detailed analysis of each of these processes, starting from the regime of laser melting.

The threshold fluence for surface melting of a bulk EAM Ni target has been determined[58] to be 36 mJ/cm^2. In all simulations performed between absorbed fluences of 36 and 172 mJ/cm^2, the effect of laser irradiation is found to be limited to the melting of a surface region of the target followed by epitaxial resolidification. At the highest fluence in the melting regime, 172 mJ/cm^2, material ejection is limited to 10 atoms (5% of a monolayer) evaporated from the transiently melted surface of the target. The conditions leading to the fast melting in this simulation can be analyzed on the basis of the temperature and pressure distributions shown in Figure 1a. A relatively strong, as compared to other metals, electron−phonon coupling in Ni results in a rapid energy transfer from the hot electrons excited by the laser pulse to the lattice. The initial fast lattice heating is largely confined within the top 50 nm region of the target (Figure 1a). The temperature of the lattice in the surface region quickly exceeds the melting temperature of the EAM Ni material, leading to fast melting of more than a 50 nm part of the target within the first 30 ps after the laser pulse. Fast melting is followed by a much slower melting of an additional 15 nm layer within ∼500 ps and resolidification that completes by the time of 2.4 ns.

A detailed atomic-level analysis of the melting process demonstrates that the fast component of the melting process corresponds to homogeneous nucleation and growth of multiple liquid regions inside the overheated crystal, whereas the slower component of the melting process is characterized by propagation of a well-defined liquid-crystal interface formed by the end of the homogeneous melting process deeper into the target. The picture of the two-stage melting process observed in this simulation is consistent with earlier observations of the competition between the homogeneous and heterogeneous melting mechanisms in MD simulations of short pulse laser interactions with Ni, Au, and Al films[50,60,61] as well as with the results of time-resolved reflectivity measurements[62] revealing fast (5−10 ps) and slow (100s ps) melting stages for GaAs irradiated by a femtosecond pulse in the "thermal melting" regime. A two-stage laser-induced melting process has also been reported for Ag films deposited on a MgO substrate.[63,64] The short time scales of the first (∼5 ps) and second (∼25 ps) stages of the melting process, however, suggests that the second stage is likely to correspond to the formation of a liquid−crystal interface at the boundary of the homogeneously melted region, rather than propagation of the well-defined melting front deeper into the target. The time scales of melting (∼30 ps)[63] and resolidification (∼200−300 ps)[64] as well as the melting depth of ∼20−30 nm, estimated in these pump−probe experiments, are consistent with

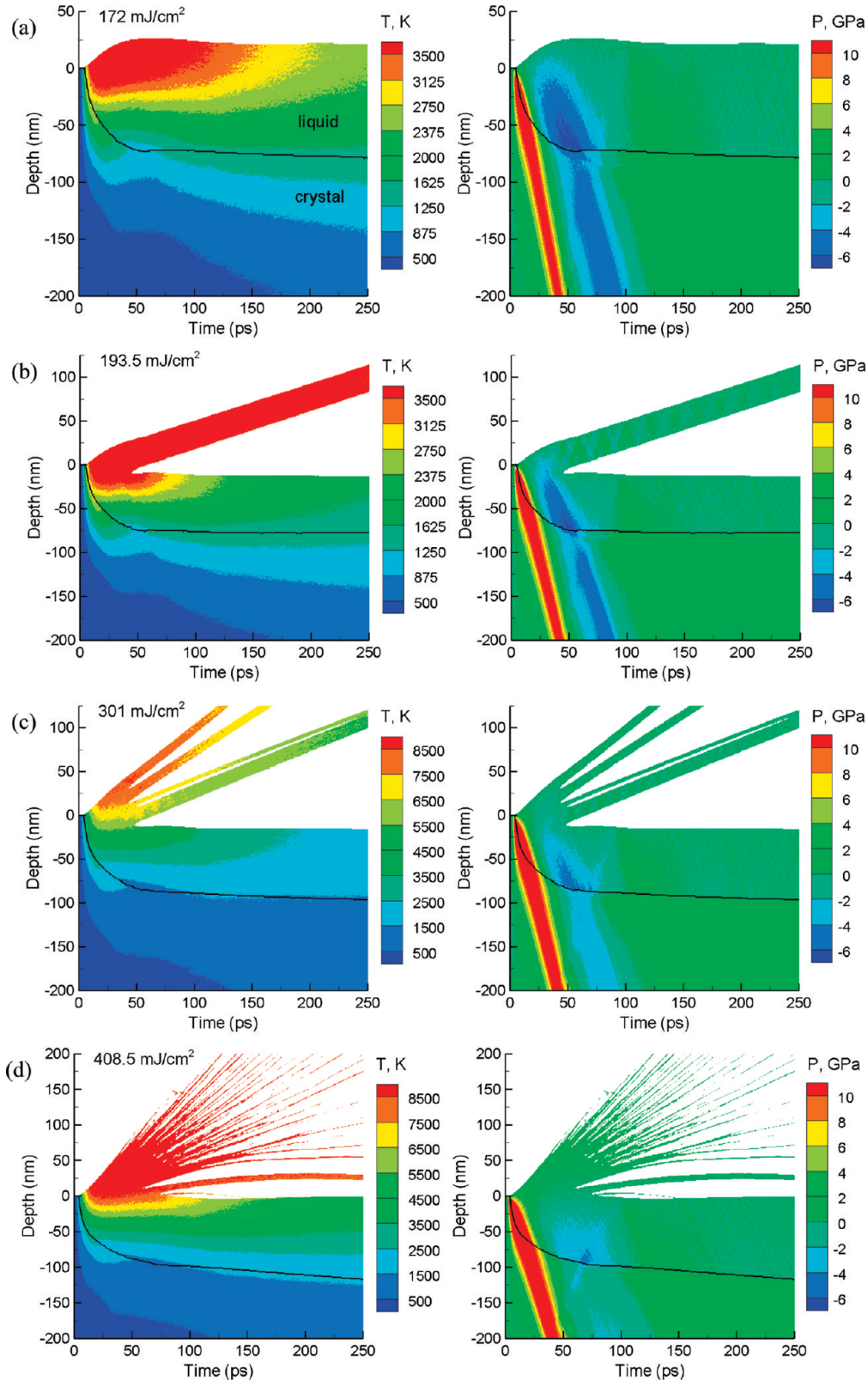

Figure 1. Temperature (left) and pressure (right) contour plots in simulations of a bulk Ni target irradiated with 1 ps laser pulses. Laser pulses have Gaussian temporal profiles with peak intensities reached at 2.5 ps from the beginning of the simulations. Values of the absorbed fluence used in the simulations are 172 mJ/cm^2 (a), 193.5 mJ/cm^2 (b), 301 mJ/cm^2 (c), and 408.5 mJ/cm^2 (d). Laser pulses are directed along the *Y*-axes from the top of the contour plots. Black lines separate the melted regions from crystalline parts of the target. Areas where the density of the material is less than 10% of the initial density before the irradiation are not shown in the plots. Note the difference in the scales of the temperature contour maps used in panels a,b and c,d.

the results of the simulations performed at fluences close to the threshold for laser melting.

The evolution of the melting and resolidification processes is illustrated in Figure 2a, where the amount of the melted

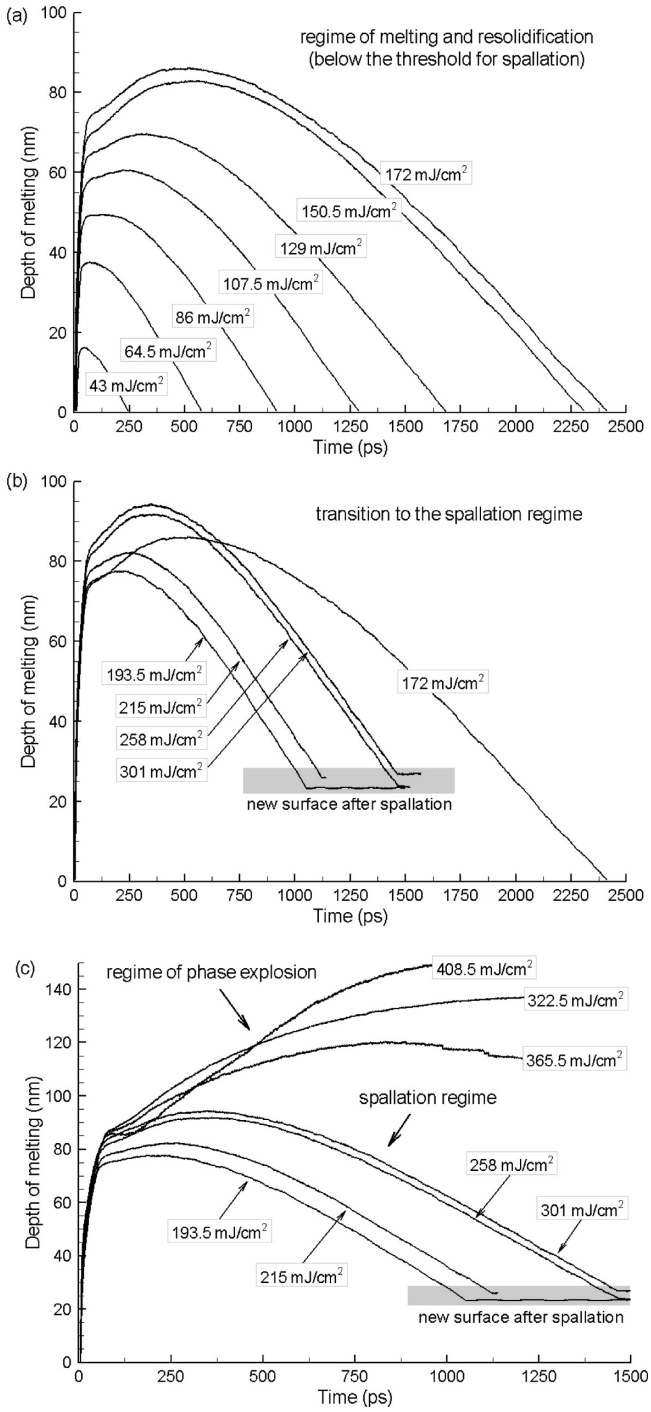

Figure 2. Evolution of the melting depth in simulations performed for a bulk Ni target irradiated with 1 ps laser pulses. Results obtained in the regime of surface melting and resolidification, below the threshold for laser spallation, are shown in panel a. Changes in melting behavior upon the transitions to the spallation regime and from the spallation regime to the phase explosion regime are illustrated in panels b and c, respectively. Depth of melting is expressed in units of depth in the initial target (a layer of this depth in the initial target has the number of atoms equal to those in the melted layer).

material is shown as a function of time for several laser fluences below the threshold for material removal from the target. Two types of melting curves can be distinguished in Figure 2a. At laser fluences below 86 mJ/cm^2, the fast homogeneous melting of a surface layer is immediately followed by epitaxial recrystallization. At fluences above 86 mJ/cm^2, two-stage melting, similar to the one described above for the fluence of 172 mJ/cm^2, takes place. The transition from purely homogeneous melting at low fluences to two-stage melting at higher fluences can be explained as follows. At low fluences, fast homogeneous melting results in formation of the liquid−crystal interface within the top 50 nm layer of the target, which is the layer heated during the time of the initial electron−phonon equilibration ($L_c \approx 50$ nm in Ni).[58] Heat conduction to the bulk of the target leads to cooling of the liquid−crystal interface below the melting temperature, causing resolidification. At higher fluences, above 86 mJ/cm^2, the liquid−crystal interface formed by the end of the homogeneous melting process is located deeper than the 50 nm layer containing most of the energy deposited by the laser pulse. Heat flow from the hot surface layer deeper into the bulk of the target proceeds through the liquid−crystal interface, heating the interface to a higher temperature (e.g., temperature plot in Figure 1a) and pushing the melting front deeper into the target.

As soon as the temperature at the liquid−crystal interface drops below the melting temperature of EAM Ni, T_m, the direction of the interface propagation changes and the melted region starts to shrink due to resolidification (Figure 2a). The velocity of resolidification increases with increasing undercooling below the melting temperature and reaches the maximum value by the time the melting front reaches the surface of the target. The local temperature of the liquid-crystal interface is also affected by the release of the heat of crystallization and is higher than the temperature of the surrounding material on both sides of the interface. The temperature of the interface at the end of the resolidification process is ranging from $\sim$0.83 T_m at a fluence of 43 mJ/cm^2 to $\sim$0.9 T_m at a fluence of 172 mJ/cm^2. The corresponding maximum velocity of the resolidification front changes from $\sim$110 m/s at 43 mJ/cm^2 to $\sim$60 m/s at 172 mJ/cm^2. These values of the solidification velocities are comparable to those estimated from pump−probe measurements performed for Ag films.[64]

Turning to the analysis of the pressure evolution in Figure 1a, the fast temperature increase occurring under conditions of stress confinement (see Section 2) leads to the buildup of high compressive pressure, which in turn relaxes by driving a compressive pressure wave deeper into the bulk of the target and inducing an unloading tensile wave that follows the compressive component. The compressive and tensile components of the pressure wave propagate without any noticeable reflection from the boundary separating the MD and continuum parts of the model, indicating that the pressure-transmitting boundary condition is working properly. After the laser-induced pressure wave leaves the surface area of the target, zero pressure quickly establishes in the melted region. The thermoelastic stresses in the crystalline part of the target, however, do not relax completely, with some residual quasi-static compressive stresses present below the liquid−crystal interface (the transition from zero pressure in the melted part of the target to a positive pressure in the crystalline part is more apparent in Figure 6, where a more narrow scale is used in the pressure contour map). The origin of these quasi-static compressive stresses can be explained by the confinement of the heated crystalline material in the lateral (parallel to the surface) directions. For a typical laser spot diameter of $\sim$100 μm, relaxation of the laser-induced thermoelastic stresses can only proceed in the direction normal to the surface. These conditions of lateral confinement are correctly reproduced by the periodic boundary conditions applied in the simulations in the directions parallel to the surface. In the melted part of the target, the stresses remain isotropic during the uniaxial expansion of the surface region, and the pressure

quickly relaxes down to zero. The uniaxial expansion of the crystalline part of the target, however, results in anisotropic lattice deformations and corresponding anisotropic stresses. Complete relaxation of these anisotropic thermoelastic stresses cannot be achieved by uniaxial expansion of the crystal, resulting in the residual stresses that remain in the surface region of the target as long as the temperature of the irradiated surface exceeds the temperature of the bulk of the target. The pressure is defined as a negative one-third of the first invariant of the stress tensor, and the positive value of pressure in the crystalline part of the target contains different contributions from different diagonal components of the stress tensor.

The increase in the laser fluence above 172 mJ/cm^2 results in a separation of a layer of melted material from the bulk of the target (Figure 1b). As briefly discussed below, the ejection of the liquid layer is driven by the relaxation of the laser-induced stresses generated in the surface region of the target under conditions of stress confinement. Therefore, by analogy with the term "spallation" commonly used to describe the dynamic fracture that results from the reflection of a shock wave from a back surface of a sample,[65,66] the material ejection due to the laser-induced stresses is called here front surface laser spallation. The separation and ejection of the liquid layer takes place by the nucleation, growth, and coalescence of multiple voids in a subsurface region of the target. The appearance of the voids coincides with the arrival of the unloading tensile wave that propagates from the surface and increases its strength with depth. The mechanical stability of the region subjected to the void nucleation is strongly affected by laser heating, and therefore, the depth of the spallation region is much closer to the surface as compared with the depth where the maximum tensile stresses are generated (Figure 1b).

Although in the simulation the ejected liquid layer is stabilized by the use of the periodic boundary conditions, one can expect a rapid decomposition of the layer into liquid droplets under experimental conditions, where the variation of local fluence within the laser spot and dynamics of the layer separation from the target are likely to cause disruptions in the thin liquid shell expanding from the irradiated area of the target. The results of earlier MD simulations of laser irradiation of bulk molecular targets,[16,17,29,67] metal films,[50,68−70] bulk metal targets,[16,71] and systems where interatomic interaction is described by Lennard-Jones potential[72−74] suggest that the photomechanical spallation is a general process that can occur in a wide class of materials and different types of targets. The mechanisms of spallation are found to be similar in molecular and metal targets and are described in detail in ref 16.

An increase in the laser fluence above the spallation threshold results in the separation and ejection of multiple layers and/or droplets from the target as illustrated by the results obtained for a laser fluence of 301 mJ/cm^2 (Figure 1c). At this fluence, the surface layer is strongly overheated and readily disintegrates at moderate tensile stresses. The temperature of the surface region of the target, however, still remains below the temperature required for the onset of phase explosion. Following a method applied earlier to a system of Ar atoms[75] and a molecular system represented by the breathing sphere model,[31] we determined the threshold temperature for the onset of phase explosion for the EAM Ni material in constant pressure MD simulations of a slow heating of a metastable liquid. The threshold temperature for the phase explosion, found to be between 9000 and 9500 K at zero pressure for EAM Ni, manifests itself by the onset of the phase separation and a sharp increase in the volume of the system. The threshold temperature for phase explosion can be expected to be ∼10% below the critical temperature of the material. The estimations of the value of the critical temperature of Ni reported in the literature (e.g., 9576 K,[76] 9100 K,[77] and 7585 K[78]) are in a reasonable agreement with the value that can be estimated from the threshold temperature for phase explosion predicted with the EAM Ni potential.

The maximum surface temperature realized in the simulation performed at 301 mJ/cm^2 does not reach this threshold temperature and without the assistance of the tensile stresses associated with the unloading wave the material ejection would be limited to the evaporation of individual atoms from the surface. Therefore, despite the relatively high laser fluence and surface temperature, we still classify the process leading to the ejection of the liquid droplets in this simulation as spallation.

Further increase in the laser fluence leads to an abrupt change in the characteristics of the ablation process. At laser fluence above ∼320 mJ/cm^2, the surface region of the irradiated target reaches the threshold temperature for phase explosion and rapid decomposition of the overheated material into a mixture of vapor and liquid droplets becomes the main process responsible for the material ejection. An example illustrating this ablation mechanism is shown in Figure 1d, where the temperature and pressure contour plots are shown for a simulation performed at an absorbed fluence of 408.5 mJ/cm^2. A surface region where temperature exceeds or approaches the threshold temperature for phase explosion becomes unstable and disintegrates in an explosive manner.

The difference in the characteristics of the ejection process in the spallation and phase explosion regimes leads to a question on whether the transition between these two regimes is a gradual one (the layers or droplets ejected in the spallation regime become smaller, and the amount of the vapor phase gradually increases with fluence) or there is an abrupt change in the dominant mechanism responsible for the material ejection. To answer this question we consider the fluence dependence of the total amount of material removed from the target (total ablation yield) and the number of ejected individual (vapor-phase) atoms (Figure 3). While the transition from spallation to phase explosion does not result in an increase in the total amount of the material removed from the target (Figure 3a), it is signified by a sharp, threshold-like increase in the number of the vapor-phase atoms in the ablation plume (Figure 3b). Thus, we can conclude that there is an abrupt transition from spallation to phase explosion at a well-defined threshold fluence. Above the threshold fluence, the main driving force for the decomposition and collective ejection (ablation) of the overheated layer of the target is provided by an explosive release of a large amount of vapor, rather than the relaxation of photomechanical stresses.

The spontaneous decomposition of the overheated material into a mixture of vapor-phase atoms and liquid droplets, observed in the simulations performed at high fluences, is consistent with the phase explosion mechanism predicted on the basis of the classical nucleation theory[6−9] and confirmed in earlier simulations of laser ablation.[17,23,26−31] A peculiarity of phase explosion occurring under conditions of stress confinement is that it takes place simultaneously with the relaxation of the laser-induced stresses, resulting in a more vigorous material ejection and higher ablation yields as compared to a "pure" phase explosion, which is characteristic for longer pulses (see Section 3.4).

The observation that the total ablation yield does not increase upon the transition from the spallation to phase explosion regime (Figure 3a) can be explained by a higher energy cost of the decomposition of the surface region of

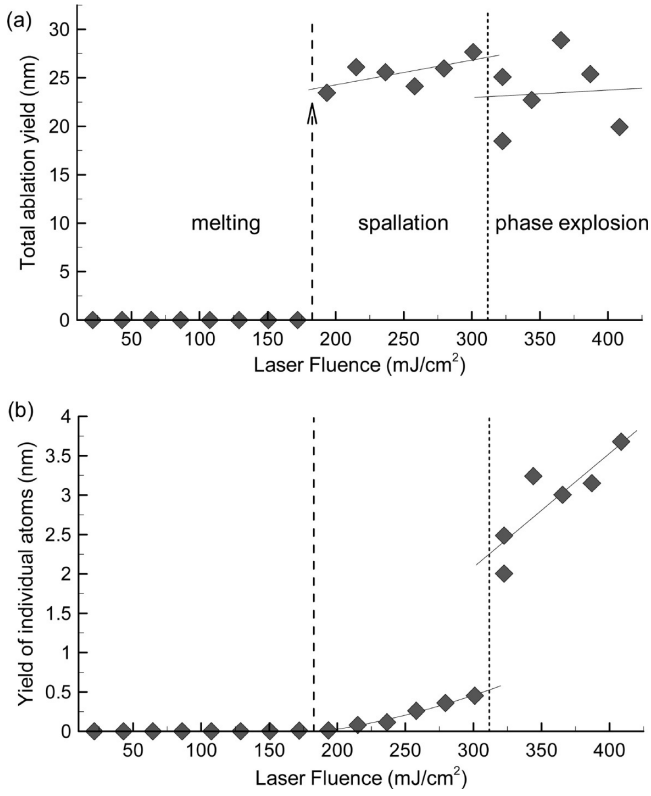

Figure 3. Total ablation yield (a) and number of individual (vapor-phase) atoms in the ablation plume (b) as functions of the absorbed laser fluence. Results are for simulations of a bulk Ni target irradiated with 1 ps laser pulses, with an ablation plume analyzed at 500 ps from the beginning of the simulations. Values of the total yield and yield of individual atoms are expressed in units of depth in the initial target (a layer of this depth in the initial target has the number of atoms equal to those ejected from the target). Dashed lines and arrows mark the threshold fluences for spallation and phase explosion.

the target into a mixture of vapor and small liquid droplets as compared to the ejection of large liquid layers and droplets in the spallation regime. Moreover, in the phase explosion regime, some of the droplets ejected with small initial velocities can be pushed back to the target by the pressure from the expanding vapor component of the plume. For example, a deceleration of the largest droplet ejected in the simulation performed with a fluence of 408.5 mJ/cm^2 is apparent in Figure 1d, leading to the eventual redeposition of the droplet. As a result, the total ablation yield just above the threshold for the onset of phase explosion is, on average, even lower than the yield observed below the threshold, in the spallation regime (Figure 3a).

The drastic change in the composition of the ejected ablation plume, from relatively large (nanometers) liquid droplets and a negligible fraction of individual atoms (less than 2% of the total yield) to a mixture of smaller droplets or clusters and a much larger fraction of the vapor-phase atoms (more than 10%), can be related to the results of recent plume imaging experiments[79] where the maximum ejection of nanoparticles in laser ablation of Ni targets is observed at low fluences, whereas the degree of the plume atomization increases at higher fluences. An opposite trend, however, is reported for Cu and Au,[80,81] where a large fraction of the ablated material is atomized at low fluences and the transition to the high-fluence regime corresponds to an increase in the efficiency of nanoparticle generation. The contradictory experimental results suggest the need for further investigation of the material-dependent characteristics of the ablation process.

The transition from spallation to phase explosion can also be related to the experimental observation of the disappearance of optical interference patterns (Newton rings), observed in pump−probe experiments,[74,82] with an increase in laser fluence. The observation of the Newton rings has been explained by the spallation of a thin liquid layer from the irradiated target,[16,73,83] whereas the disappearance of the interference fringes in the central part of the laser spot[74] may be related to the transition to the phase explosion regime.

3.2. Effect of Spallation and Phase Explosion on Melting and Resolidification. The threshold fluence for photomechanical spallation of a Ni target (~180 mJ/cm^2) is five times higher than the threshold for surface melting (36 mJ/cm^2). The maximum melting depth is steadily growing with fluence in the melting regime and reaches the depth of 86 nm at a fluence of 172 mJ/cm^2 (Figure 4a). The contribution of heterogeneous melting to the total amount of the melted material is relatively small, and melting depth is mainly defined by the fast homogeneous melting of the strongly overheated surface region of the target during the first tens of picoseconds (Figure 2a). At the same time, the presence of the heterogeneous stage of the melting process increases the time when the melting depth reaches its maximum up to hundreds of picoseconds (Figure 4b). The time required for complete resolidification of the surface region increases almost linearly with fluence and reaches a value of 2.4 ns at a fluence of 172 mJ/cm^2 (Figure 4c).

At the spallation threshold, the maximum melting depth, time when the melting depth reaches its maximum value, and time required for complete resolidification all decrease abruptly (Figures 2b and 4). This observation can be explained by the interruption of the electronic heat conduction from the hot surface layer separated from the bulk of the target (Figure 1b). As a result, the amount of heat transferred to the liquid−crystal interface from the surface region decreases, the second (slow, heterogeneous) stage of the melting process shortens, and the maximum melting depth drops. Because the fast homogeneous stage of melting, which is the main contributor to the total melting depth, is not affected by the spallation, the drop in the maximum melting depth is relatively small (Figure 4a). The spallation of the hot surface layer, however, makes a much stronger impact on the kinetics of the melting and resolidification processes (Figure 2b), with the time of the maximum melting and time required for complete resolidification dropping by more than a factor of 2 at the spallation threshold (Figure 4b,c).

The transition from the spallation to phase explosion regime results in another abrupt change in the characteristics of the melting and resolidification processes (Figures 2c and 4), and this time in the opposite direction, where the time of the maximum melting and the time required for complete resolidification increase by more than a factor of 2. However, the maximum depth of melting experiences a more moderate increase at the threshold for phase explosion. Because the change in the total ablation yield at the threshold for phase explosion is relatively small (Figure 3a), the dramatic change in the kinetics of the melting and resolidification processes (Figure 2c) cannot be explained simply by the removal of the heat deposited in the ablated part of the target. The difference in the material ejection mechanisms in the two regimes is clearly playing an important role in causing the changes in the characteristics of the melting and resolidification processes. In the case of spallation, the energy transfer from the ejected liquid layer(s) or large droplets is interrupted as soon as they separate from the target. In the case of phase explosion, the ablation plume contains a substantial fraction of vapor (Figure 3b), which

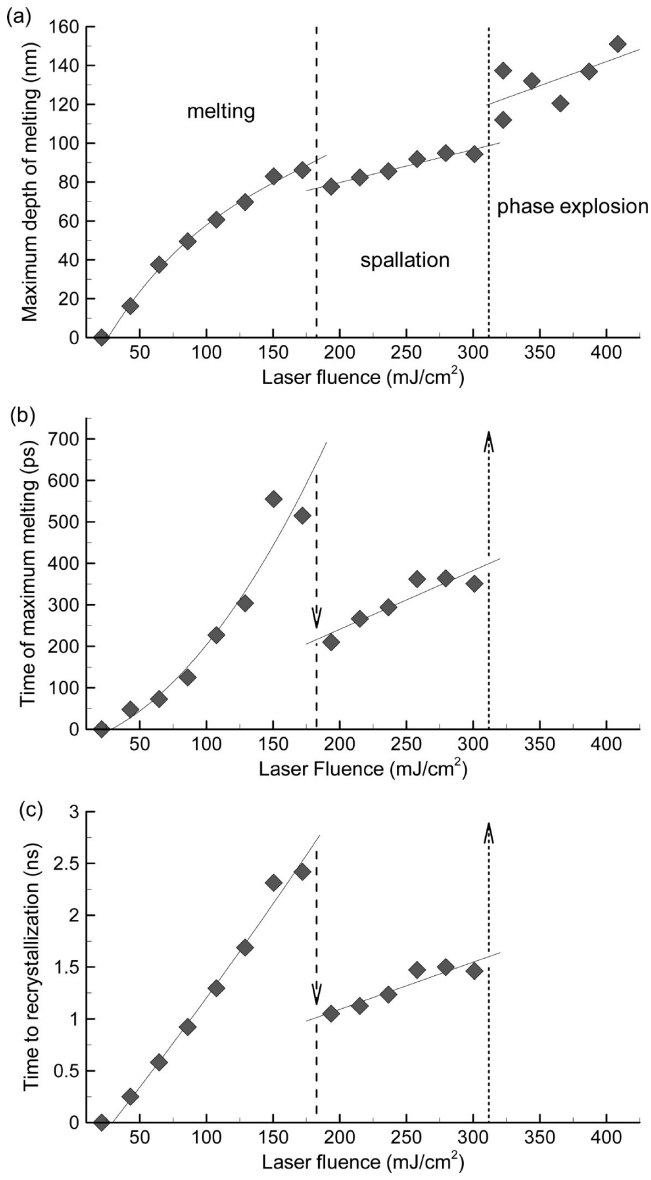

Figure 4. Maximum melting depth (a), time when the melted depth reaches its maximum value (b), and time required for complete resolidification of the melted surface region (c) as functions of the absorbed laser fluence. Results are for simulations of a bulk Ni target irradiated with 1 ps laser pulses. Melting depth is expressed in units of depth in the initial target (a layer of this depth in the initial target has the number of atoms equal to those in the melted layer). The dashed lines and arrows mark the threshold fluences for spallation and phase explosion. In all simulations performed at fluences that correspond to the regime of phase explosion, the time when the maximum melting depth is reached exceeds 750 ps and the time required for complete resolidification exceeds 3 ns.

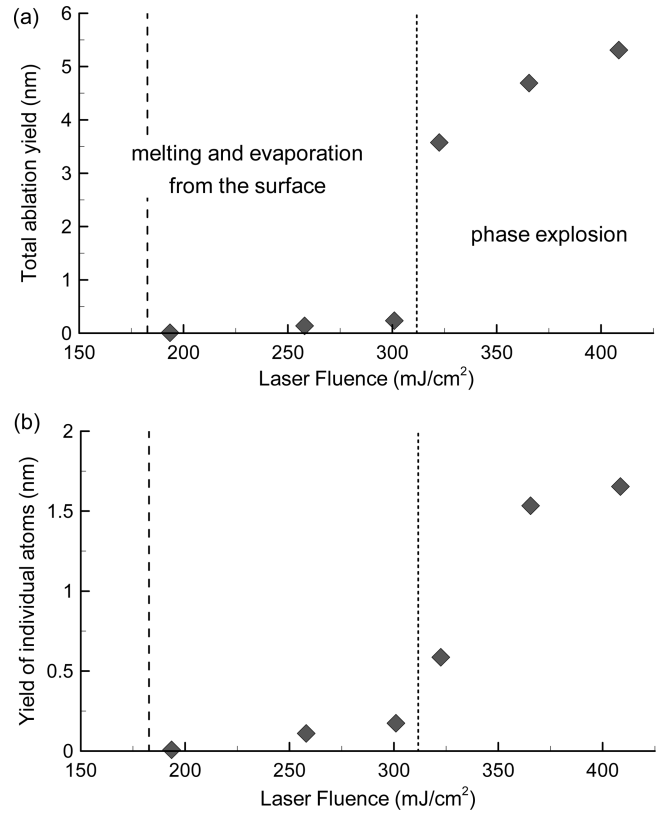

Figure 5. Total ablation yield (a) and number of individual (gas-phase) atoms in the ablation plume (b) as functions of absorbed laser fluence. Results are for simulations of a bulk Ni target irradiated with 50 ps laser pulses, with ablation plume analyzed at 620 ps from the beginning of the simulations. Values of the total yield and yield of individual atoms are expressed in units of depth in the initial target (a layer of this depth in the initial target has the number of atoms equal to those ejected from the target). The dashed lines mark the threshold fluences for spallation and phase explosion identified in simulations performed with 1 ps laser pulses (Figure 3).

continues to interact with the target long after the explosive decomposition and ejection of the overheated layer. This interaction slows down the cooling of the surface and significantly prolongs the time scales of the melting and resolidification processes. The contribution of the slow propagation of the melting front (heterogeneous melting) to the overall melting process starts to be comparable to the fast homogeneous melting in the phase explosion regime (Figure 2c).

While the depth of the melted layer on the order of 100 nm, predicted in the simulations, is consistent with most of the experimental observations,[34−36,84−86] there have been reports suggesting a much larger, on the order of a micrometer, thickness of the molten layer in femtosecond laser drilling experiments.[14] A possible contribution of a nanosecond component (pedestal pulse) of a femtosecond laser pulse generated by a commercial laser system has been suggested to explain the substantial melting observed in these experiments.[14,87]

3.3. On the Possible Contribution of Melt Expulsion to the Ablation Yield. As the laser fluence increases above the threshold for phase explosion, the fraction of the vapor phase in the ablation plume increases as well (Figure 3). Under experimental conditions of finite-size laser spot, the pressure exerted by the expanding ablation plume on the melted layer can cause a redistribution of the melted material and formation of a rim of resolidified material along the edges of the laser spot[18,14,35,37,39,40] as well as an expulsion of the melt. The relaxation of the initial laser-induced pressure, generated under conditions of stress confinement (see Section 3.1), can also make a contribution to the initiation of an active flow within the melted part of the target.[46] The onset of the melt expulsion at the threshold for phase explosion, in particular, can be related to the experimental observation of two ablation regimes, commonly reported for femtosecond and picosecond laser ablation of metals.[86,88−90] The fluence dependence of the ablation depth is found to be well described by two logarithmic dependences, $d = l\ln(F/F_{th}^{l})$ with different values of the characteristic length of the laser energy deposition, l, and the corresponding threshold fluence, F_{th}^{l}, used in the two regimes. At low fluences, the energy transfer out of the optical penetration depth is neglected and the characteristic length of the energy deposition is assumed to

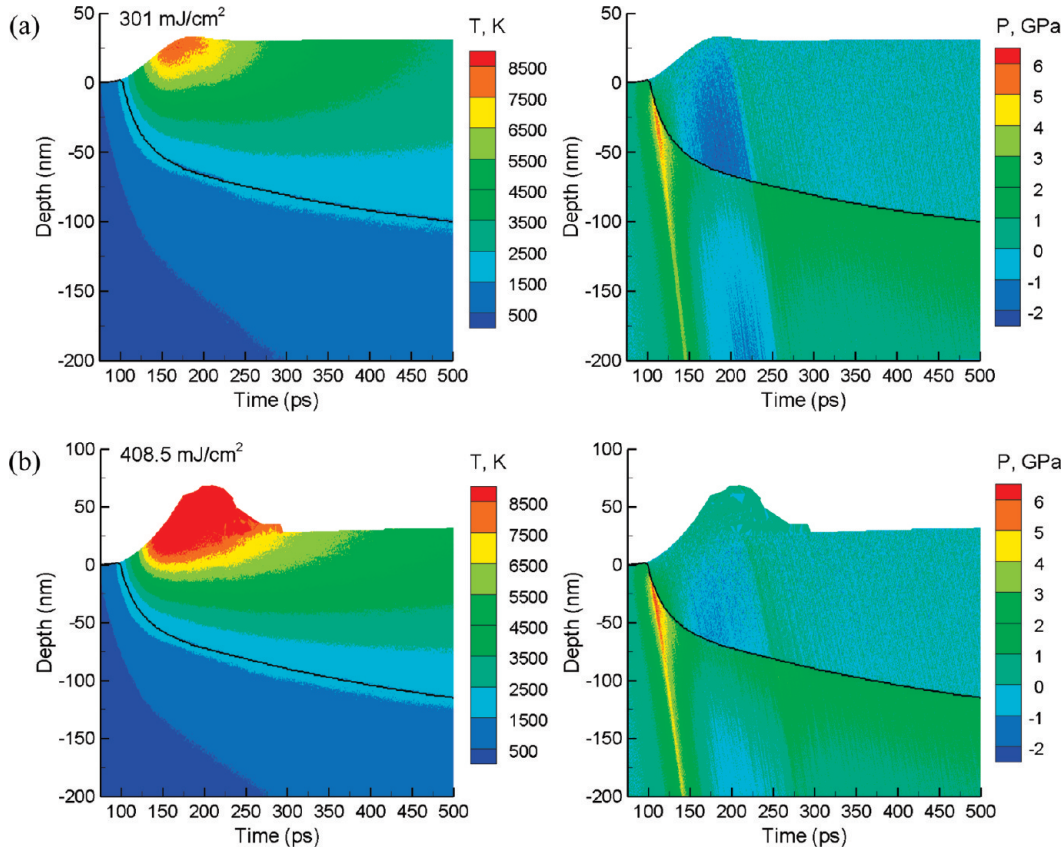

Figure 6. Temperature (left) and pressure (right) contour plots in simulations of a bulk Ni target irradiated with 50 ps laser pulses. Laser pulses have Gaussian temporal profiles with peak intensities reached at 125 ps from the beginning of the simulations. Values of the absorbed fluence used in the simulations are 301 mJ/cm^2 (a) and 408.5 mJ/cm^2 (b). Laser pulses are directed along the *Y*-axes from the top of the contour plots. Black lines separate the melted regions from crystalline parts of the target. Areas where the density of the material is less than 10% of the initial density before the irradiation are not shown in the plots.

be equal to the optical penetration depth, whereas in the higher fluence regime the electron thermal diffusion length is used in the description of the experimental data.[86,88,89]

The results of the simulations suggest an alternative explanation for the experimental observations, which does not require an assumption on the energy confinement within the optical absorption depth at low laser fluences. In the low fluence regime, the experimental values of the ablation depth are limited to a few tens of nanometers and exhibit a weak fluence dependence, which is consistent with the ablation yield observed in the simulations performed in the spallation regime (Figure 3a). At higher fluences, the experimental ablation depth exhibits a stronger logarithmic dependence on the laser fluence, with values of the ablation depth per pulse increasing up to 100 nm and more. Although we do not observe such an increase in the ablation yield in the simulations, the experimental values of the ablation depth in the high-fluence regime are on the order of the melting depth predicted in the simulations (Figure 4a). Moreover, the fluence dependence of the melting depth is consistent with the experimental logarithmic dependences observed for the ablation depth. Thus, a possible explanation of the transition to the high-fluence regime with an ablation yield on the order of 100 nm is the onset of the melt expulsion due to the recoil pressure exerted by the ablation plume in the phase explosion regime. The melt expulsion cannot be observed in the TTM-MD simulations reported in this work because of the absence of the pressure gradients in the lateral directions; the periodic boundary conditions used in the simulations are effectively representing a situation of an "infinitely large" laser spot.

The notion of melt expulsion contributing to the ablation yield in the phase explosion regime can be supported by the observation of the appearance of the traces of the molten material upon the transition from the low-fluence regime (attributed here to spallation) to the high-fluence regime (attributed here to phase explosion and melt expulsion)[86] as well as by the observation of large (tens of nanometers) droplets in the high-fluence regime of femtosecond laser ablation of Ni targets.[91] The complete melt expulsion has also been assumed in interpretation of experimental ablation characteristics obtained with longer, 40 ps, laser pulses,[35] when the contribution of photomechanical effects is likely to be negligible (see Section 3.4).

3.4. From Melting to Phase Explosion in the Absence of Stress Confinement. In order to highlight the role of the photomechanical effects in defining the characteristics of the laser-induced processes in simulations discussed above for irradiation with 1 ps laser pulses, the results from these simulations are compared here with the ones obtained with longer, 50 ps, laser pulses. As discussed in Section 2, the condition for stress confinement is satisfied for a pulse duration of 1 ps but not for 50 ps. Therefore, one can expect that the effects related to the relaxation of the laser-induced stresses will be substantially reduced in the simulations performed with 50 ps pulses. Indeed, the fluence dependence of the total yield, shown in Figure 5a, exhibits the complete absence of the spallation regime. In the range of fluences where spallation is observed with 1 ps pulses, from ~180 mJ/cm^2 to ~320 mJ/cm^2 (Figure 3a), the material ejection with 50 ps laser pulses is limited to evaporation from the melted surface of the target.

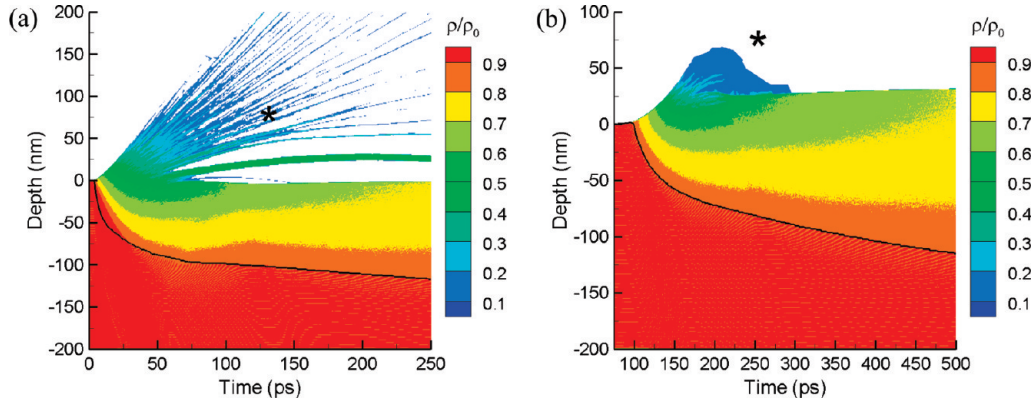

Figure 7. Density contour plots in simulations of a bulk Ni target irradiated with 1 ps (a) and 50 ps (b) laser pulses. Laser pulses have Gaussian temporal profiles with peak intensities reached at 2.5 ps (a) and 125 ps (b) from the beginning of the simulations. The value of the absorbed fluence used in both simulations is 408.5 mJ/cm^2. Laser pulses are directed along the *Y*-axes from the top of the contour plots. Black lines separate the melted regions from crystalline parts of the target. The density scale is normalized to the initial density before the irradiation, ρ_0. Areas where the density of the material is less than $0.1\rho_0$ are not shown in the plots. Black stars show the locations in the plume and times for which snapshots are shown in Figure 8.

The reason for the absence of spallation in the simulations performed with 50 ps pulses is apparent from a comparison between the pressure plots shown for simulations performed at the same laser fluence of 301 mJ/cm^2 with 1 and 50 ps pulses (Figures 1c and 6a). In the case of a 50 ps laser pulse, the surface region has sufficient time to expand during the laser heating (absence of stress confinement) and the strength of the laser-induced pressure wave is reduced down to a level that cannot cause spallation (note the difference in the scales of the pressure contour maps used in Figures 1c and 6a).

The ablation yield increases sharply at about the same threshold fluence at which the transition from spallation to phase explosion is observed in the simulations performed with 1 ps pulses. The increase in the total yield is accompanied by an increase in the number of ejected individual atoms (Figure 5b), suggesting that similar to the phase explosion observed with 1 ps irradiation the explosive decomposition of the overheated surface region into vapor, small liquid droplets and clusters takes place above the threshold fluence. The values of the ablation yield, however, are several times smaller in the case of the longer pulses. The difference in the ablation yield observed with the two pulse durations in the phase explosion regime can be explained by two factors.

First, the characteristic heat diffusion depth, estimated for the time equal to the pulse duration of 50 ps, $z_{diff} = (2K_0\tau_p/C_l)^{1/2} \approx 40$ nm (an assumption of electron−lattice equilibrium, $T_e = T_l$, and the value of the lattice heat capacity of the EAM Ni material at the melting temperature, $C_l = 5 \times 10^6$ Jm^{-3} K^{-1}, are used in the estimation), is comparable to the depth of the initial lattice heating during the time of the electron−phonon equilibration, $L_c \approx 50$ nm. Therefore, some moderate cooling of the surface region due to the energy transfer to the bulk of the target by electronic heat conduction can take place during the 50 ps laser pulse. This cooling, however, is relatively small and does not have any significant effect on the maximum temperatures achieved by the end of the laser pulses. In particular, similar maximum surface temperatures can be seen in the temperature contour plots shown in Figures 1c and 6a for the simulations performed with 1 and 50 ps laser pulses.

The second and more important factor responsible for the higher values of the ablation yield in the simulations performed with the shorter laser pulse is the contribution of the thermoelastic stresses, generated under conditions of stress confinement, to the material ejection. In the case of a 50 ps laser pulse, the material ejection in the regime of phase explosion is fueled by the release of the vapor phase alone, whereas in the case of a 1 ps pulse, the relaxation of the laser-induced stresses and explosive release of vapor are taking place simultaneously and are acting in accord, leading to a more vigorous material ejection.

The effect of stress confinement on the ejection process is also reflected in the composition of the ablation plume. The ablation plume ejected in the regime of stress confinement includes a large number of liquid droplets, with traces of the droplets clearly visible in the contour plots shown in Figures 1d and 7a. Such traces are not present in the plots shown for the simulation performed for the same laser fluence with 50 ps laser pulse (Figures 6b and 7b). The contour plots are made by dividing the system into 1 nm layers and calculating the average properties (temperature, pressure, and density) for layers where the density of the material is above 10% of the initial density of the solid target, ρ_0. The hump in the contour plots shown in Figures 6b and 7b corresponds to the initial stage of the expansion of a cloud of vapor and small clusters, with the density of the cloud quickly falling below $0.1\rho_0$ upon expansion. To illustrate the difference in the composition of the ablation plume generated upon irradiation with 1 and 50 ps laser pulses, snapshots of the plume taken at the same height above the initial surface and the same time after the peak intensities of the laser pulses are shown in Figure 8. In the simulation performed with a 1 ps pulse, the plume includes a large number of liquid droplets, with the vapor phase constituting less than 20% of the total number of ejected atoms. In the case of a 50 ps pulse, the plume consists of vapor and small clusters, with more than 30% of the ejected material being in the vapor phase.

A similar effect of stress confinement has been observed earlier in MD simulations of laser ablation of molecular targets,[17,29,30] where a higher ablation yield, larger droplets, and higher ejection velocities are predicted in simulations performed for irradiation conditions of stress confinement. The "weaker" phase explosion observed with the longer laser pulse is also consistent with the results of recent MD simulations of nanosecond ($\tau_p = 11.3$ ns) laser ablation of a Lennard−Jones system,[92] where a transition from the intensive surface evaporation to phase explosion of an overheated surface layer has been identified from the onset of the ejection of small liquid droplets. In a simulation performed close to the threshold fluence for phase explosion, evaporation is still the dominant process, with

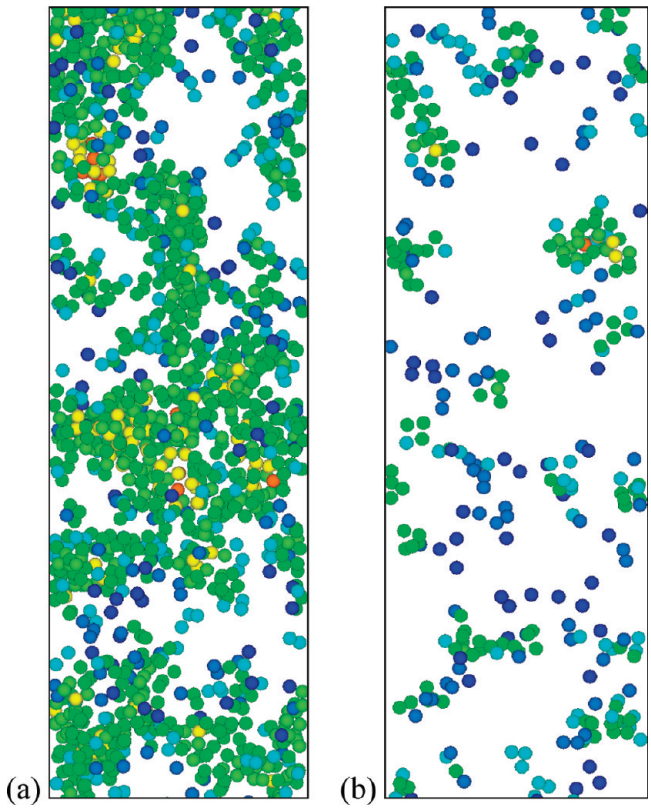

Figure 8. Snapshots of ablation plumes generated in the simulations performed with 1 ps (a) and 50 ps (b) laser pulses and the same laser fluence of 408.5 mJ/cm^2. Snapshots in panels a and b are taken at times and locations marked by black stars in panels a and b of Figure 7, respectively. Atoms are colored according to their potential energies, from the blue color corresponding to a zero potential energy of an individual atom to the red color corresponding to the potential energy of an atom in a crystal.

droplets constituting a relatively small fraction of the total ablation yield.[92]

The experimental observation of an increase in the ablation threshold fluence and a decrease in the ablation depth with a pulse width increasing from the femtosecond range to tens of picoseconds[86] is consistent with the results of the simulations, predicting a substantial reduction of the ablation yield as the pulse width changes from 1 to 50 ps (Figures 3a and 5a). The appearance of pronounced traces of molten material in the picosecond irradiation regime[18,35,36,93] can also be related to the results of the simulations. While in the phase explosion regime the values of the maximum melting depth predicted in the two series of simulations are close to each other, the time of the melting and resolidification cycle is substantially longer in simulations performed with 50 ps laser pulses, providing the conditions for more significant redistribution of the melt within the laser spot (rim formation) and facilitating the expulsion of the melt.

In the absence of any significant contribution of the laser-induced thermoelastic stresses to the material ejection in the simulations performed with 50 ps laser pulses, the transition from surface evaporation to the collective material ejection (ablation) is mainly defined by the evolution of the thermodynamic parameters in the surface region of the target. The temperature and pressure contour plots, shown in Figure 6, demonstrate that the compressive stresses generated at the beginning of the laser heating process trigger the expansion of the surface layer that continues during the remaining part of the heating process. The heating time is sufficiently long to ensure that the pressure remains at a low level as the temperature of the surface region increases. Decomposition of the surface region into vapor and liquid droplets starts when the surface temperature reaches the threshold temperature for phase explosion, defined in Section 3.1. This threshold temperature is not reached in a simulation performed at 301 mJ/cm^2 (Figure 6a) but is exceeded in the simulation performed at 408.5 mJ/cm^2 (Figure 6b).

To provide a more clear demonstration of the thermodynamic conditions leading to the onset of phase explosion, it may be instructive to plot the evolution of the surface temperature and pressure in the form of pressure−temperature phase diagrams, similar to the ones used in theoretical analysis of the explosive boiling process.[6−9] The time evolution of the values of temperature and pressure, averaged over the atoms that are initially located in the top 5 nm surface region of the target, are shown for three simulations performed with 50 ps laser pulses in Figure 9. The size of the region for which the "thermodynamic trajectories" are shown is close to the size of the region ejected in the phase explosion regime (Figure 5a). The equilibrium melting line and threshold temperature for phase explosion are shown by the dashed and dashed−dotted lines in the diagram. The melting line is calculated in liquid−crystal coexistence simulations,[60] whereas the threshold temperature for phase explosion is estimated in a series of slow heating constant pressure simulations as explained in Section 3.1. Note that the loss of thermodynamic stability of the superheated liquid and onset of explosive boiling can be expected to take place at temperatures ∼10% below the liquid spinodal.[6−9] Although we did not determine the precise critical point parameters of the EAM Ni material, the values estimated from the threshold temperature for phase explosion can be related to the values of the critical temperature and pressure obtained by fitting experimental data to model equations of state (9576 K and 1.116 GPa,[76] 9100 K and 0.9 GPa,[77] and 7585 K and 1.05 GPa[78]) as well as the critical point parameters predicted for a model Ni material in MD simulations performed with a pairwise interatomic potential (9460 K and 1.08 GPa).[94]

In all simulations, the initial temperature increase up to the melting temperature leads to a rise of the compressive pressure that reaches its maximum value by the time of ∼100 ps (note that the peak intensity of the laser pulse corresponds to the time of 125 ps). The pressure increase can be explained by two factors: (1) the finite time needed for the relaxation of the thermoelastic stresses created by the initial heating of ∼50 nm surface region of the target and (2) the inability of the crystalline target to completely relax the thermoelastic stresses by the uniaxial expansion in the direction normal to the surface. For the top 5 nm surface layer, the time of mechanical relaxation (expansion) is on the order of 1 ps, and therefore, the second factor, related to the confinement of the crystal lattice in the lateral directions and discussed in more details in Section 3.1, is the dominant one. Indeed, the melting of the surface region removes the conditions responsible for keeping the anisotropic stresses in the crystal, and the pressure quickly relaxes down to a low level defined by the balance between continued laser heating and expansion of the melted layer. The remaining part of the heating process proceeds at low values of pressure and brings the temperature to the superheating region and close to the threshold temperature for phase explosion. The threshold temperature is not reached in the simulation performed at 301 mJ/cm^2 (Figure 9a), and the material ejection is limited in this case to the evaporation from the surface. In the simulation

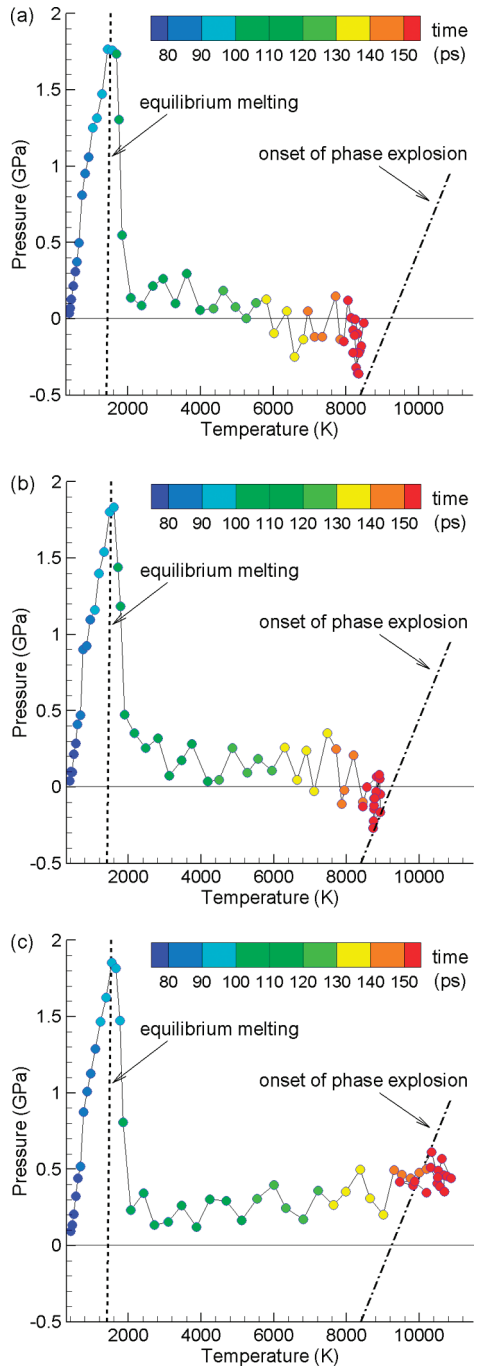

Figure 9. Pressure−temperature diagrams calculated for the first 180 ps of the simulations performed with 50 ps laser pulses at absorbed fluences of 301 (a), 322.5 (b), and 408.5 mJ/cm^2 (c). Values of temperature and pressure are averaged over the surface region occupied by atoms that belong to the top 5 nm layer of the original target. The data points shown by circles are colored from blue to red in the order of increasing time. The laser pulse peak intensity is reached at a time of 125 ps. Dashed and dashed−dotted lines show the equilibrium melting line (calculated in liquid−crystal coexistence simulations[60]) and the threshold temperature for phase explosion (estimated as explained in the text). Temperature and pressure contour plots corresponding to the diagrams in panels a and c are shown in Figure 6.

performed at 322.5 mJ/cm^2 (Figure 9b), the average temperature of the 5 nm layer of the target is barely reaching the threshold temperature, but the temperature of the top part of this layer exceeds the threshold, triggering explosive decomposition and ejection of a part of the surface layer that corresponds to a depth of ∼3.5 nm in the original target (Figure 5a). Further increase in the laser fluence leads to a stronger overheating of the surface layer (e.g., Figure 9c) and an increase in the amount of the ejected material (Figure 5a).

Results of the analysis of thermodynamic conditions leading to the onset of the explosive boiling or phase explosion in the simulations are consistent with the theoretical analysis of this phenomenon based on the classical nucleation theory[6−9] but are in a sharp contradiction with the conclusion of ref 95, where the conditions for phase explosion are inferred to be impossible to achieve in laser ablation of metals and semiconductors with laser pulses longer than ∼10 ps. The evolution of pressure and temperature shown in Figure 9 is also very different from the "thermodynamic trajectory" obtained in a recent simulation of nanosecond laser ablation,[96] where an almost linear increase in pressure in a subsurface region of the irradiated target is observed during the nanosecond laser pulse, reaching the maximum values that are almost 2 orders of magnitude higher than the critical pressure. This result is likely to be related to the peculiar thermodynamic properties of the two-dimensional (2D) hexagonal close-packed crystals used in the simulations. In particular, the 2D crystal is observed to be heated significantly above the critical temperature of the 2D system without crossing the crystal−liquid coexistence line of the phase diagram.[72,96] The confinement of the heated 2D crystal in the direction parallel to the surface, rather than a decrease in the speed of sound by 2 orders of magnitude,[96] could be the reason for the pressure build up during the nanosecond laser pulse observed in this simulation. The application of the predictions of the 2D model to real materials, therefore, should be done with caution. In particular, the contour plots shown in Figure 6b demonstrate a quick and complete relaxation of the laser-induced stresses in the melted part of the target and presence of relatively low quasi-static compressive stresses in the crystalline part of the target. There are no reasons to expect that, with increasing pulse duration, the compressive pressure in the melted part of the target would become much stronger and would exceed the equilibrium vapor pressure prior to the onset of the phase decomposition and ablation. The conventional phase explosion model, thus, is likely to be appropriate in the nanosecond irradiation regime as well. Indeed, no anomalies related to the build up and relaxation of the laser-induced pressure are observed in MD simulations of nanosecond laser material interaction performed with a more realistic three-dimensional model.[92] The temperature−pressure conditions leading to the ablation of a Ni target, determined in nanosecond laser ablation experiments,[97] also suggest that the pressure stays below the liquid−gas coexistence curve, confirming the conventional phase explosion mechanism.

4. Conclusions

The results of a series of atomistic computer simulations of short pulse laser melting and ablation of metal targets reveal a complex picture of interrelated processes and physical mechanisms responsible for the laser-induced structural transformations and material removal from the targets. At low laser fluences, the processes induced by the short pulse laser irradiation are found to be limited to the melting of a surface region of the target followed by an epitaxial regrowth of the crystalline bulk of the target and complete resolidification on a time scale from hundreds of picoseconds to several nanoseconds. The kinetics of the melting process is defined by the relative contributions of the homogeneous and heterogeneous melting mechanisms. At laser fluences close to the threshold for surface melting, fast homogeneous melting (nucleation and growth of

multiple liquid regions within the overheated crystal) takes place during the first several tens of picoseconds and is immediately followed by the resolidification process. At higher laser fluences, the melting proceeds in two stages, with fast homogeneous melting followed by slower heterogeneous melting (propagation of a well-defined liquid−crystal interface deeper into the target) that takes several hundreds of picoseconds.

For sufficiently short laser pulses, under the condition of stress confinement, fast laser energy deposition results in the build up of strong compressive stresses in the surface region of the target. The relaxation of the laser-induced compressive stresses generates an unloading (tensile) wave propagating from the surface to the bulk of the target. When laser fluence reaches a well-defined spallation threshold value, tensile stresses become sufficiently strong to induce nucleation, growth, and coalescence of multiple voids in the surface region of the target, leading to separation (spallation) and ejection of a liquid layer. As the laser fluence increases above the spallation threshold, photomechanical disruption of the melted region of the target can result in the ejection of multiple layers and/or large liquid droplets.

A transition to the third fluence regime identified in the simulations (the regime of phase explosion) is signified by an abrupt change in the composition of the ejected plume, from liquid layers and large droplets to a mixture of individual atoms, small clusters and droplets. The sharp (threshold-like) increase in the amount of the vapor-phase atoms at the transition from photomechanical spallation to the phase explosion regime reflects the difference in the physical mechanisms responsible for the material ejection in these two regimes. An explosive release of vapor, rather than the relaxation of photomechanical stresses, provides the main driving force for the collective ejection of the overheated layer of the target in the regime of phase explosion.

The processes of laser melting, spallation, and phase explosion are taking place simultaneously and are closely intertwined with each other. In particular, the onset of spallation interrupts the heat conduction from the hot surface layer separated from the bulk the target, leading to a sharp drop in the maximum melting depth and duration of the melting process. The transition to phase explosion has an opposite effect on the melting and resolidification processes; the duration of the melting and resolidification cycle as well as the size of the melting zone increase due to the continued interaction of the ablation plume with the surface of the target. The stronger interaction of the ablation plume with the surface of the target indicates that the transition to the phase explosion regime may also result in the onset of the melt expulsion due to the pressure exerted by the expanding ablation plume. Although the effect of the melt expulsion is not present in the simulations performed with periodic boundary conditions (corresponding to an "infinitely large" laser spot with uniform spatial distribution of fluence), it would provide an explanation for the experimentally observed steep increase in the ablation yield at higher fluences.

A comparison of the results obtained in the simulations performed with 1 and 50 ps laser pulses reveals a strong effect of the laser-induced stresses generated in the regime of stress confinement on the characteristics of the ablation process. No spallation is observed in the simulations performed with 50 ps laser pulses where the condition for stress confinement is not satisfied. Moreover, phase explosion is "weaker" in these simulations, resulting in smaller values of the ablation yield and larger fractions of the vapor phase in the ejected plume. The more "vigorous" material ejection with higher ablation yields, observed in the simulations performed with the shorter laser pulse, can be explained by the synergistic contribution of the laser-induced stresses and the explosive release of vapor in phase explosion occurring under conditions of stress confinement.

Acknowledgment. Financial support is provided by the National Science Foundation through the Thermal Transport and Thermal Processes Program of the Chemical, Bioengineering, Environmental, and Transport Systems Division (Award CTS-0348503).

References and Notes

(1) Bäuerle, D. *Laser Processing and Chemistry*; Springer-Verlag: Berlin, Heidelberg, 2000.
(2) von Allmen, M.; Blatter, A.; *Laser Beam Interactions with Materials*; Springer-Verlag: Berlin, Heidelberg, 1998.
(3) *Pulsed Laser Deposition of Thin Films*; Chrisey, D. B., Hubler, G. K., Eds.; Wiley-Interscience: New York, 1994.
(4) Phipps, C. R.; Luke, J. R.; McDuff, G. G.; Lippert, T. *Appl. Phys. A: Mater. Sci. Process.* **2003**, *77*, 193.
(5) Anisimov, S. I. *Sov. Phys. JETP* **1968**, *27*, 182.
(6) Martynyuk, M. M. *Sov. Phys. Tech. Phys.* **1976**, *21*, 430.
(7) Miotello, A.; Kelly, R. *Appl. Phys. Lett.* **1995**, *67*, 3535.
(8) Miotello, A.; Kelly, R. *Appl. Phys. A: Mater. Sci. Process.* **1999**, *69*, S67.
(9) Bulgakova, N. M.; Bulgakov, A. V. *Appl. Phys. A: Mater. Sci. Process.* **2001**, *73*, 199.
(10) Bennett, T. D.; Grigoropoulos, C. P.; Krajnovich, D. J. *J. Appl. Phys.* **1995**, *77*, 849.
(11) Brailovsky, A. B.; Gaponov, S. V.; Luchin, V. I. *Appl. Phys. A: Mater. Sci. Process.* **1995**, *61*, 81.
(12) von Allmen, M. *J. Appl. Phys.* **1976**, *47*, 5460.
(13) Zweig, A. D. *J. Appl. Phys.* **1991**, *70*, 1684.
(14) Semak, V. V.; Thomas, J. G.; Campbell, B. R. *J. Phys. D: Appl. Phys.* **2004**, *37*, 2925.
(15) Paltauf, G.; Dyer, P. E. *Chem. Rev.* **2003**, *103*, 487.
(16) Leveugle, E.; Ivanov, D. S.; Zhigilei, L. V. *Appl. Phys. A: Mater. Sci. Process.* **2004**, *79*, 1643.
(17) Zhigilei, L. V.; Garrison, B. J. *J. Appl. Phys.* **2000**, *88*, 1281.
(18) Yang, J.; Zhao, Y.; Zhang, N.; Liang, Y.; Wang, M. *Phys. Rev. B* **2007**, *76*, 165430.
(19) Masuhara, H.; Asahi, T.; Hosokawa, Y. *Pure Appl. Chem.* **2006**, *78*, 2205.
(20) Hatanaka, K.; Tsuboi, Y.; Fukumura, H.; Masuhara, H. *J. Phys. Chem. B* **2002**, *106*, 3049.
(21) Bulgakova, N. M.; Stoian, R.; Rosenfeld, A.; Hertel, I. V.; Marine, W.; Campbell, E. E. B. *Appl. Phys. A: Mater. Sci. Process.* **2005**, *81*, 345.
(22) Song, K. H.; Xu, X. *Appl. Surf. Sci.* **1998**, *127*−*129*, 111.
(23) Cheng, C.; Xu, X. *Phys. Rev. B* **2005**, *72*, 165415.
(24) Porneala, C.; Willis, D. A. *Appl. Phys. Lett.* **2006**, *89*, 211121.
(25) Yoo, J. H.; Jeong, S. H.; Mao, X. L.; Greif, R.; Russo, R. E. *Appl. Phys. Lett.* **2000**, *76*, 783.
(26) Povarnitsyn, M. E.; Itina, T. E.; Sentis, M.; Khishchenko, K. V.; Levashov, P. R. *Phys. Rev. B* **2007**, *75*, 235414.
(27) Povarnitsyn, M. E.; Khishchenko, K. V.; Levashov, P. R. *Appl. Surf. Sci.* **2009**, *255*, 5120.
(28) Zhigilei, L. V.; Kodali, P. B. S.; Garrison, B. J. *Chem. Phys. Lett.* **1997**, *276*, 269.
(29) Zhigilei, L. V.; Leveugle, E.; Garrison, B. J.; Yingling, Y. G.; Zeifman, M. I. *Chem. Rev.* **2003**, *103*, 321.
(30) Zhigilei, L. V. *Appl. Phys. A: Mater. Sci. Process.* **2003**, *76*, 339.
(31) Leveugle, E.; Zhigilei, L. V. *J. Appl. Phys.* **2007**, *102*, 074914.
(32) Vogel, A.; Venugopalan, V. *Chem. Rev.* **2003**, *103*, 577.
(33) Kashii, M.; Hosokawa, Y.; Kitano, H.; Adachi, H.; Mori, Y.; Takano, K.; Matsumura, H.; Inoue, T.; Murakami, S.; Sugamoto, K.; Yoshikawa, H.; Sasaki, T.; Masuhara, H. *Appl. Surf. Sci.* **2007**, *253*, 6447.
(34) Preuss, S.; Demchuk, A.; Stuke, M. *Appl. Phys. A: Mater. Sci. Process.* **1995**, *61*, 33.
(35) Jandeleit, J.; Urbasch, G.; Hoffmann, H. D.; Treusch, H.-G.; Kreutz, E. W. *Appl. Phys. A: Mater. Sci. Process.* **1996**, *63*, 117.
(36) Chichkov, B. N.; Momma, C.; Nolte, S.; von Alvensleben, F.; Tünnermann, A. *Appl. Phys. A: Mater. Sci. Process.* **1996**, *63*, 109.
(37) Zeng, X.; Mao, X. L.; Greif, R.; Russo, R. E. *Appl. Phys. A: Mater. Sci. Process.* **2005**, *80*, 237.
(38) Tonshoff, H. K.; Momma, C.; Ostendorf, A.; Nolte, S.; Kamlage, G. *J. Laser. Appl.* **2000**, *12*, 23.
(39) Cheng, J.; Perrie, W.; Sharp, M.; Edwardson, S. P.; Semaltianos, N. G.; Dearden, G.; Watkins, K. G. *Appl. Phys. A: Mater. Sci. Process.* **2009**, *95*, 739.

(40) Ben-Yakar, A.; Harkin, A.; Ashmore, J.; Byer, R. L.; Stone, H. A. *J. Phys. D: Appl. Phys.* **2007**, *40*, 1447.
(41) Nakata, Y.; Okada, T.; Maeda, M. *Jpn. J. Appl. Phys.* **2003**, *42*, L1452.
(42) Korte, F.; Koch, J.; Chichkov, B. N. *Appl. Phys. A: Mater. Sci. Process.* **2004**, *79*, 879.
(43) Kuznetsov, A. I.; Koch, J.; Chichkov, B. N. *Appl. Phys. A: Mater. Sci. Process.* **2009**, *94*, 221.
(44) Singha, S.; Hu, Z.; Gordon, R. J. *J. Appl. Phys.* **2008**, *104*, 113520.
(45) Li, Y.; Wang, C. Y.; Ni, X. C.; Wang, Z. J.; Jia, W.; Chai, L. *Appl. Phys. Lett.* **2006**, *89*, 161110.
(46) Ivanov, D. S.; Rethfeld, B.; O'Connor, G. M.; Glynn, Th. J.; Volkov, A. N.; Zhigilei, L. V. *Appl. Phys. A: Mater. Sci. Process.* **2008**, *92*, 791.
(47) Vorobyev, A. Y.; Guo, C. *Appl. Phys. A: Mater. Sci. Process.* **2007**, *86*, 235.
(48) Lam, Y. C.; Tran, D. V.; Zheng, H. Y. *Laser Part. Beams* **2007**, *25*, 155.
(49) Anisimov, S. I.; Kapeliovich, B. L.; Perel'man, T. L. *Sov. Phys. JETP* **1974**, *39*, 375.
(50) Ivanov, D. S.; Zhigilei, L. V. *Phys. Rev. B* **2003**, *68*, 064114.
(51) The use of terms "lattice" and "lattice temperature" in this paper does not imply the preservation of the crystalline order in the system. By using these terms, we merely follow the terminology established in the literature presenting TTM calculations, when the term lattice temperature is commonly used to refer to the temperature of the ionic subsystem that can be brought out of equilibrium with the conduction band electrons by short pulse laser irradiation.
(52) Zhigilei, L. V.; Garrison, B. J. In *Multiscale Modelling of Materials*, MRS Symposia Proceedings No. 538, Materials Research Society, Pittsburgh, PA, 1999; pp 491−496.
(53) Schäfer, C.; Urbassek, H. M.; Zhigilei, L. V.; Garrison, B. J. *Comput. Mater. Sci.* **2002**, *24*, 421.
(54) Zhou, X. W.; Wadley, H. N. G.; Johnson, R. A.; Larson, D. J.; Tabat, N.; Cerezo, A.; Petford-Long, A. K.; Smith, G. D. W.; Clifton, P. H.; Martens, R. L.; Kelly, T. F. *Acta Mater.* **2001**, *49*, 4005.
(55) *American Institute of Physics Handbook*, 3rd ed.; McGraw-Hill: New York, 1972.
(56) Lin, Z.; Zhigilei, L. V.; Celli, V. *Phys. Rev. B* **2008**, *77*, 075133.
(57) Lin, Z.; Zhigilei, L. V. *Appl. Surf. Sci.* **2007**, *253*, 6295.
(58) Ivanov, D. S.; Zhigilei, L. V. *Appl. Phys. A: Mater. Sci. Process.* **2004**, *79*, 977.
(59) Ivanov, D. S.; Zhigilei, L. V. *Phys. Rev. Lett.* **2007**, *98*, 195701.
(60) Ivanov, D. S.; Zhigilei, L. V. *Phys. Rev. Lett.* **2003**, *91*, 105701.
(61) Lin, Z.; Zhigilei, L. V. *Phys. Rev. B* **2006**, *73*, 184113.
(62) Sokolowski-Tinten, K.; Bialkowski, J.; Boing, M.; Cavalleri, A.; von der Linde, D. *Phys. Rev. B* **1998**, *58*, R11805.
(63) Chan, W.-L.; Averback, R. S.; Cahill, D. G.; Lagoutchev, A. *Phys. Rev. B* **2008**, *78*, 214107.
(64) Chan, W.-L.; Averback, R. S.; Cahill, D. G.; Ashkenazy, Y. *Phys. Rev. Lett.* **2009**, *102*, 095701.
(65) Fortov, V. E.; Kostin, V. V.; Eliezer, S. *J. Appl. Phys.* **1991**, *70*, 4524.
(66) Tamura, H.; Kohama, T.; Kondo, K.; Yoshida, M. *J. Appl. Phys.* **2001**, *89*, 3520.
(67) Zhidkov, A. G.; Zhigilei, L. V.; Sasaki, A.; Tajima, T. *Appl. Phys. A: Mater. Sci. Process.* **2001**, *73*, 741.
(68) Zhigilei, L. V.; Ivanov, D. S.; Leveugle, E.; Sadigh, B.; Bringa, E. M. In *High-Power Laser Ablation V*; Phipps, C. R., Ed.; Proceedings of SPIE, 2004, Vol. 5448, pp 505−519.
(69) Upadhyay, A. K.; Urbassek, H. M. *J. Phys. D: Appl. Phys.* **2005**, *38*, 2933.
(70) Upadhyay, A. K.; Inogamov, N. A.; Rethfeld, B.; Urbassek, H. M. *Phys. Rev. B* **2008**, *78*, 045437.
(71) Schäfer, C.; Urbassek, H. M.; Zhigilei, L. V. *Phys. Rev. B* **2002**, *66*, 115404.
(72) Perez, D.; Lewis, L. J. *Phys. Rev. B* **2003**, *67*, 184102.
(73) Anisimov, S. I.; Zhakhovskii, V. V.; Inogamov, N. A.; Nishihara, K.; Oparin, A. M.; Petrov, Yu. V. *JETP Lett.* **2003**, *77*, 606.
(74) Agranat, M. B.; Anisimov, S. I.; Ashitkov, S. I.; Zhakhovskii, V. V.; Inogamov, N. A.; Nishihara, K.; Petrov, Yu. V.; Fortov, V. E.; Khokhlov, V. A. *Appl. Surf. Sci.* **2007**, *253*, 6276.
(75) Garrison, B. J.; Itina, T. E.; Zhigilei, L. V. *Phys. Rev. E* **2003**, *68*, 041501.
(76) Young, D. A.; Alder, B. J. *Phys. Rev. A* **1971**, *3*, 364.
(77) Nikolaev, D. N.; Ternovoi, V. Ya.; Pyalling, A. A.; Filimonov, A. S. *Int. J. Thermophys.* **2002**, *23*, 1311.
(78) Fortov, V. E.; Lomonosov, I. V. *Pure Appl. Chem.* **1997**, *69*, 893.
(79) Amoruso, S.; Bruzzese, R.; Pagano, C.; Wang, X. *Appl. Phys. A: Mater. Sci. Process.* **2007**, *89*, 1017.
(80) Noël, S.; Hermann, J.; Itina, T. *Appl. Surf. Sci.* **2007**, *253*, 6310.
(81) Hermann, J.; Noël, S.; Itina, T. E.; Axente, E.; Povarnitsyn, M. E. *Laser Phys.* **2008**, *18*, 374.
(82) Sokolowski-Tinten, K.; Bialkowski, J.; Cavalleri, A.; von der Linde, D.; Oparin, A.; Meyer-ter-Vehn, J.; Anisimov, S. I. *Phys. Rev. Lett.* **1998**, *81*, 224.
(83) Inogamov, N. A.; Petrov, Y. V.; Anisimov, S. I.; Oparin, A. M.; Shaposhnikov, N. V.; von der Linde, D.; Meyer-ter-Vehn, J. *JETP Lett.* **1999**, *69*, 310.
(84) Le Harzic, R.; Huot, N.; Audouard, E.; Jonin, C.; Laporte, P.; Valette, S.; Fraczkiewicz, A.; Fortunier, R. *Appl. Phys. Lett.* **2002**, *80*, 3886.
(85) Feng, Q.; Picard, Y. N.; Liu, H.; Yalisove, S. M.; Mourou, G.; Pollock, T. M. *Scripta Mater.* **2005**, *53*, 511.
(86) Nolte, S.; Momma, C.; Jacobs, H.; Tünnermann, A.; Chichkov, B. N.; Wellegehausen, B.; Welling, H. *J. Opt. Soc. Am. B* **1997**, *14*, 2716.
(87) Semak, V. V.; Campbell, B. R.; Thomas, J. G. *J. Phys. D: Appl. Phys.* **2006**, *39*, 3440.
(88) Furusawa, K.; Takahashi, K.; Kumagai, H.; Midorikawa, K.; Obara, M. *Appl. Phys. A: Mater. Sci. Process.* **1999**, *69*, S359.
(89) Mannion, P. T.; Magee, J.; Coyne, E.; O'Connor, G. M.; Glynn, T. J. *Appl. Surf. Sci.* **2004**, *233*, 275.
(90) Mannion, P. T.; Favre, S.; Mullan, C.; Ivanov, D. S.; O'Connor, G. M.; Glynn, T. J.; Doggett, B.; Lunney, J. G. *J. Phys.: Conf. Ser.* **2007**, *59*, 753.
(91) Liu, B.; Hu, Z.; Che, Y.; Chen, Y.; Pan, X. *Appl. Phys. Lett.* **2007**, *90*, 044103.
(92) Zhang, L.; Wang, X. *Appl. Surf. Sci.* **2008**, *255*, 3097.
(93) Ancona, A.; Nodop, D.; Limpert, J.; Nolte, S.; Tünnermann, A. *Appl. Phys. A: Mater. Sci. Process.* **2009**, *94*, 19.
(94) Cheng, C.; Xu, X. *Int. J. Thermophys.* **2007**, *28*, 9.
(95) Lorazo, P.; Lewis, L. J.; Meunier, M. *Phys. Rev. Lett.* **2003**, *91*, 225502.
(96) Perez, D.; Lewis, L. J.; Lorazo, P.; Meunier, M. *Appl. Phys. Lett.* **2006**, *89*, 141907.
(97) Xu, X.; Song, K. *Appl. Phys. A: Mater. Sci. Process.* **1999**, *69*, S869.

JP902294M